# Effect of Post-Weld Heat Treatment on Microstructural Evolution and Abrasive Wear of Nanostructured Fe-Based Hardfacing

*J. Gramajo[a]\* , A. Gualco[a,b], H. Svoboda[b,c]*

*[a]Universidad Nacional de Lomas de Zamora, Facultad de Ingeniería, Buenos Aires, Argentina.*
*[b]Consejo Nacional de Investigaciones Científicas Técnicas (CONICET), Buenos Aires, Argentina.*
*[c]Universidad de Buenos Aires (UBA), Facultad de Ingeniería, Av. Las Heras, 2214 (1427), Buenos Aires, Argentina.*

New multi-component alloys have been recently developed for applications in coatings deposited by welding. These microstructures consist on the precipitates of ultra-hard carbo-borides in a matrix with high hardness. Post-weld heat treatment is a relevant aspect to adjusting the final propierties of the deposit. In the present work, the microstructural evolution, phase properties and resistance to abrasive wear of a Fe-Cr-Nb-B-C-Si-Mn alloy deposited on a low carbon steel by semi-automatic welding process were studied. The samples were heat treated for 3 hours at temperatures between 500 and 900 °C. They were compared with respect to the samples "as welded". The microstructure was analized by scanning electron microscopy, X-ray diffraction and transmission electron microscopy. A microstructure formed by tetragonal carboborides $M_2B$ and niobium carbides, with a microhardness of 1800 HV and 2440 HV, respectively, in a matrix formed by high hardness martensite (870 HV) was observed. The post-weld heat treatment produced the tempering of the martensite and the precipitation of secondary carbides from 500 to 800 °C, producing a decrease in hardness with increasing temperature. In the specimen heat-treated at 900 °C, the hardness increased at 1130 HV, reaching higher values than those obtained in the "welded" condition (940 HV), due to the formation of martensite and $M_{23}X_6$ carbides. A linear relationship was found between hardness and abrasive wear rate.

**Keywords**: *Hardfacing, Flux-Cored Arc Welding, post-weld heat treatment, abrasive wear.*

## 1. Introduction

The application of hard coatings on elements of mining and oil drilling machines has experienced an important advance in the development of Fe-Cr-Nb-B-C-Si-Mn alloys that improve the behavior against abrasive wear with respect to the Fe-Cr-C system[1,2]. The replacement of $M_7C_3$ carbides (1400 - 1600HV) by $M_2B$ (1600-2000 HV) borides of high hardness plus a matrix with high toughness explain the improvements obtained[3,4].

The design of this alloy consisted on the empirical rules for obtaining amorphous materials. The percentage of elements in group P was approximately 7% including boron, carbon and silicon. Inoue[5-7] has reported that when any of the rules for obtaining glassy structure is not achieved, fine or nanostructured structures will be found. In this sense, the presence of 7 elements of different atomic radio, which satisfy two of the three rules, improves the ability to obtain high subcooling and consequently to obtain finer microstructures. Since the cooling rate in the welding process used is higher than the critical amorphization, a crystalline structure will be obtained.

An efficient method to surface repair or surfacing is by means of semi-automatic arc welding processes with flux cored tubular wire (FCAW)[8]. The use of inexpensive equipment and high deposition rate facilitate the implementation of these alloys.

Post-weld heat treatment (PWHT) is an efficient method to achieve the final properties of iron-based alloys[9,10].

Ye et al.[11] studied the effect of the quenching treatment in an Fe-4Cr-B alloy, obtaining that the matrix transformed to martensite with the presence of secondary carboborides $M_{23}(C,B)_6$ and that at 1100 °C showed the coalescence of carboboride. Hardness increased with increasing temperature. In this sense, the effect of PWHT could significantly affect the properties of Fe-Cr-Nb-B-C-Si-Mn multicomponent alloys, being an aspect that has been scarcely studied until now.

The objective of this work was to study the effect of PWHT temperature in nanostructured Fe-B-Cr-C-Si-Nb-Mn multicomponent alloys obtained by welding, on the microstructural evolution, the properties of the phases and the resistance to abrasive wear.

## 2. Materials and Methods

### 2.1. Welding

The consumable used was a 1.6 mm diameter tubular wire, which deposits a Fe-Cr-Nb-B-C-Si-Mn alloy. The process used was semi-automatic welding under shielding gas protection (FCAW), with a stick out of 20 mm. Table 1 shows the chemical composition specification of the manufacturer.

A test coupon was welded in a flat position, on a base plate of 150x75x12.5 mm of low carbon steel type SAE 1010.

\*e-mail: nahuel_jona@yahoo.com.ar

The welding sequence was 4 and 3 beads for the first and for the second layer respectively. The welding parameters used were 35 V and 300 A, the travel speed was 3 mm/s, and the heat input 3.5 kJ/mm. Ar-20$CO_2$ was used as shielding gas with a flow rate of 18 L / min[12].

Cross sections were extracted from the welded specimen, on which post-weld heat treatments were performed at 500, 600, 700, 800 and 900 °C, for 3 hours in all cases. The test specimens were identified based on the tempering temperature and AW (as welded) for which they were not heat treated.

## 2.2. Chemical analysis and microstructural characterization

The chemical composition was determined in the last bead by optical emission spectroscopy (OES). Boron was analyzed by plasma emission spectroscopy (PES).

The local composition of the different phases was determined using energy dispersive X-ray spectrometry (EDS).

For the different conditions analyzed, the microstructure was characterized by means of scanning electron microscopy (SEM), used secondary electron and back-scattering electron mode (BSE). The specimen surfaces were polished and etched using Vilella reagent. X-ray diffraction (XRD) on the last bead was carried out on the surface of the test coupons, using a RIGAKU equipment, with Cu K-α radiation. The scannings were carried out from 35° to 95° with a speed of 1° per minute. The phases were identified by software[13]. The phase quantifications were performed by imageJ software using five microstructures for condition.

On the AW and 500 samples, studies were carried out with a transmission electron microscope with a scanning unit (STEM) brand JEOL model JEM 2100 plus at 20 KV. For the extraction of the thin sections, the Focus Ion Beam (FIB) technique was used, Figure 1. The equipment used was a Thermo Fisher Helios NanoLab 650.

## 2.3. Microhardness and abrasive wear resistance

Measurements of Vickers hardness HV2 (20 N) on the last beads and microhardness on the phases with HV0.1 (1 N) were permormed.

In order to determine the resistance to abrasive wear of each condition, 3 samples of each were analized. The abrasion wear tests were carried out in accordance with the ASTM G65-04 "Dry Sand / Rubber Wheel" standard, according to method A[14]. The rotational speed of the rubber wheel was 200 rpm, the sand was AFS 50/70, the flow was 320 g / min and the load applied to the test specimen of 130 N. The wear was evaluated by loss of average weight of the samples, after 4309 m traveled. Some cracks were observed on the surface.

# 3. Results and Discussion

## 3.1. Chemical composition

Table 2 shows the result of the chemical analysis measured on the surface of the last bead.

The hardfacing material presented a high concentration of alloying elements, within of Fe-Cr-B-C-Nb system.

## 3.2. Macrographs

The macrograph of the cross-section bead is shown in Figure 2. The base metal and the weld metal can be seen, observing the absence of macroscopic defects, such as pores and inclusions. Transverse cracks were found which had occurred during cooling.

Based on the geometry of the beads, the dilution[5] was calculated using image analysis software (A/A+B). It was estimated at 16% with respect to subtrate.

## 3.3. Microstructural characterization

SEM images of the different conditions of last beads are shown in Figure 3.

In Figure 3a show a microstructure of the AW test specimen, where niobium carbides of size from 2 to 4 µm,

**Table 1.** Chemical composition specification of the manufacturer (% wt/wt).

| C | Mn | Si | Cr | Nb | B |
|---|---|---|---|---|---|
| <2 | <2 | <2 | <18 | <6 | <6 |

**Table 2.** Chemical composition of weld metal (% by weight).

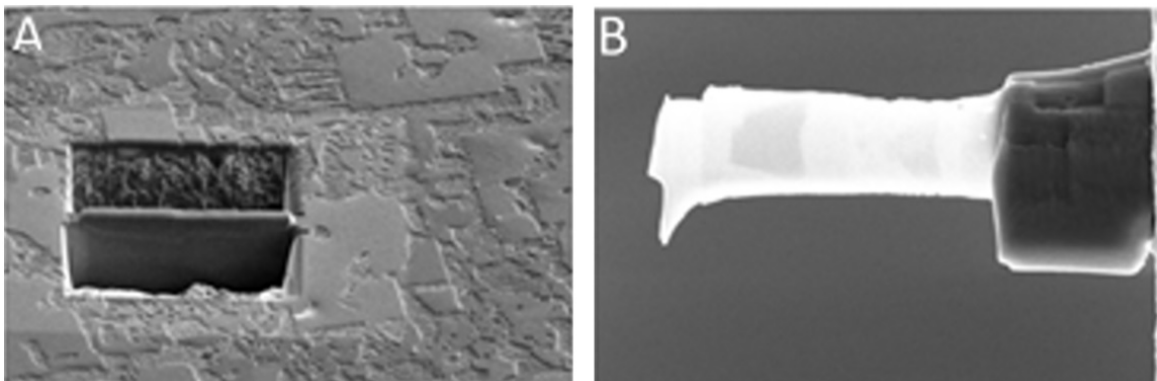| C | Mn | Si | Cr | Nb | B | Fe |
|---|---|---|---|---|---|---|
| 1,19 | 0,26 | 0,81 | 18,4 | 4,7 | 4,9 | resto |



**Figure 1.** a) Focuced Ion Beam attack on the microstructure and b) Thinned sample.

elongated carboborides $M_2B$ from 10 to 15 μm and the eutectic phase are presented. The eutectic phase is formed by flat and globular arms carboborides (II) with a thickness of 1 to 3 μm with a α'-Fe matrix and other a finer one of the coral type (I). The size of the α' phase was from 0.3 (zone II) to 10 μm (zone I). The eutectic carboborides are the $M_{23}X_6$ type, but anothers (darker areas) of $M_7X_3$ are observed. Niobium carbides of polygonal or nodular shape were observed within the $M_2B$ carboborides and between the eutectic phases. The $M_2B$ borides were presented in different configurations, being mostly block faces with right angles. It is interesting to note that block faced carboborides with right angles tend to form carbide blocks with hole. This type of morphology has been observed in $M_7C_3$ hexagonal carbides and would be associated with the spiral growth mode[15]. The presence of a halo in the surroundings of the carboboride is not observed and there is an interconnection and branching of eutectic carboborides with the primary one. Within eutectic carbides, the formation of core-shell structures composed of a core of $M_7(BC)_3$ and surrounded by $M_{23}(BC)_6$ is observed[16].

As reported in the literature[17,18], the first carbides to nucleate during the solidification process are the CNb,
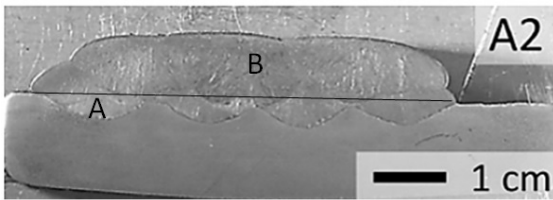


**Figure 2.** Macrograph of the welded test specimen.

with a high melting point, which can remain alone or form clusters or blocks of carbides. Later, with the decrease in temperature, $M_2B$ borides appear, which grow perpendicular to the base metal and nucleate in the area near the fusion line. On some occasions, in the areas near the surface, it can nucleate from the niobium carbides and grow in the direction of maximum heat extraction. Finally, from the remaining liquid, the eutectic or biphasic compound, α'-Fe and $M_{23}X_6$ / $M_7X_3$[17-19] is formed.

Figures 3b-e show the SEM images of the samples heat treated between 500 and 900 °C. No microstructural changes were observed in niobium carbides and in elongated borides $M_2B$ and carboborides $M_{23}BC6$. The precipitation of small carbides $M_6X$ and $M_{23}X_6$ (M = Cr, Fe; X = C, B) on the matrix α'-Fe[20] can be seen. The precipitation of carbides and carboborides that increased in size as a function of temperature was observed until reaching a maximum at 800 °C. This can be seen in the boxes in Figure 3 and in the enlargement of Figure 4.

In Fe-B-C alloys, the solubility of boron in iron is very low: 0.02 wt% in the austenite phase and 0.0004 wt% in ferrite[21,22], but due to the presence of Cr as a substitute element for Fe, the Boron solubility can reach values of 0.18-0.51% wt up to 800 °C. Röttger et al.[23] calculated that the phases present for Fe-Cr-BC ternary systems in this range of analyzed temperatures would be an FCC or BCC phase (according to temperature), $M_2B$ and $M_{23}BC_6$, being the transformation temperature from FCC to BCC close to 800 °C. In this case, due to the higher percentage of chromium and boron, said transformation temperature increases to 850°-900 °C, where the solubility and diffusivity of carbon in the FCC structure is higher than in BCC[24]. In Figure 4 it can be seen that the



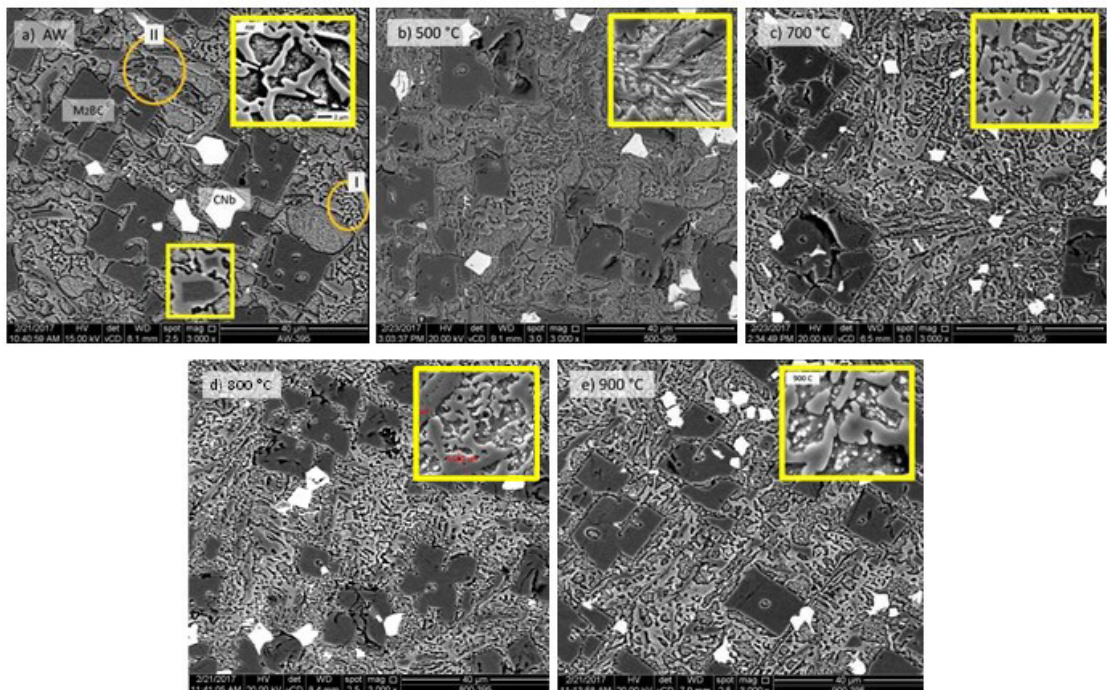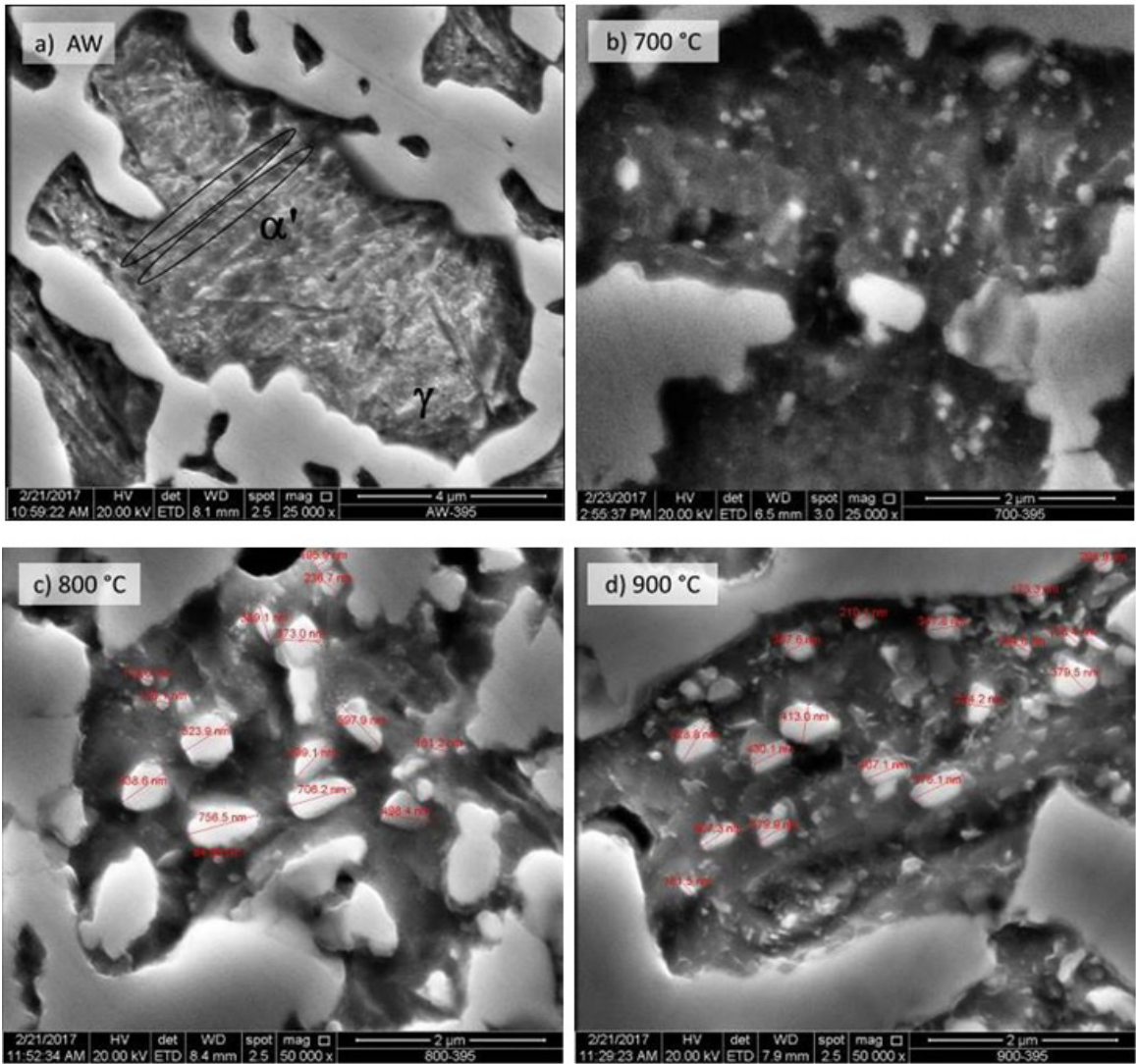**Figure 3.** BSD images of the test specimen a) AW, b) 500, c) 700, d) 800 and e) 900 °C.

**Figure 4.** Evolution of the eutectic phase a) AW, b) 700, c) 800 and d) 900 °C.

AW test specimen presented a martensite phase in a lenticular or plate shape and small fractions of retained austenite. The average size of the precipitates was 10-150 μm for the specimens treated at 500-700 °C (Figure 4b) and 400-800 μm for 800 °C (Figure 4c), which would be associated with the loss of C and B of the matrix. At 900 °C the average size of the precipitates decreased to 250-500 microns (Figure 4d). Likewise, an increase in size of the secondary carbides was observed up to 800 °C due to the migration of boron, carbon and chromium atoms for their formation and growth, from the BCC matrix. Then, with the increase in temperature to 900 °C, where the structure of the matrix changes from BCC to FCC, the dissolution of part of the carbides occurs and consequently a decrease in the average size.

In Figure 5 the X-ray diffraction spectra measured on the top of the layers, in a perpendicular direction to the substrate, are shown. The phases were identified by software.

In Figure 5 it can be seen that the microstructure was formed mainly by α'-Fe, also detecting the presence of $M_2B$ borides and metal carboborides $(Cr,Fe)_7(B,C)_3$ and $(Cr,Fe)_{23}(B,C)_6$.[9-11] A monotonic decrease of the 101 peak of the martensite and its shift towards the 110 peaks from the AW probe up to 800°C was observed. The presence of Nb carbides was detected in all the test specimens. The highly distorted α' phase for the AW test specimen presented a C and B content greater than 1.6% and 1.2% C for 500°C, respectively. After 600°C, the content decreases below 0.6% C and a single peak is observed between 42 and 45°. At 900°C at position 110 a broadening of the peak is observed due to the formation of martensite, with carbon and chromium content lower than AW and 500.

The transmission electron microscopy studies presented in Figure 6 verified that the phases present are niobium carbide with a cubic crystalline structure, carboboride $M_{23}BC_6$ of cubic lattice, iron boride and chromium $M_2B$ with a tetragonal cell and finally the highly distorted martensite with an average width near nanoscale of 100-300 μm for the AW condition. The phases found agree with those reported in

the X-ray diffraction spectra. In the sample 500, a decrease in the lattice parameters of the tetragonal martensite and a darkening product of the precipitation of coherent carbides was observed. The Fe / Cr ratio was 28/72, 83.5 / 16.5 and 94.4 / 5.6 for phases $M_2B$, $M_{23}BC_6$ and α', respectively[25]. This is consistent with the proposed mode of solidification where the first boride to form was the Cr-rich $M_2B$, then the carboborides were formed and finally the austenite phase.

Figure 7 shows the phase quantifications as a function of the AW condition and the heat-treated ones. The predominant phase is α'(M) which decreases with increasing temperature up to 800 °C, due to the presence of secondary carbides. From 800° to 900 °C there is a slight increase as a consequence of the decrease in the size of these carboborides. $M_2B$ boride, niobium carbide and eutectic carboborides do not show significant changes with heat treatment. The fluctuations are related to the dispersion between typical micrographs in these materials.

## 3.4. Microhardness

There are several methods to estimate the general mechanical properties of composite materials[26-29] where the most used are numerical simulations using the finite element method[29,30] and simple models based on the rule of mixtures[31-33]. In the present work, the latter type was used, relating the hardness of the deposit with the percentages of phases and their hardness[19], as indicated in the following equation:



**Figure 5.** XRD spectra for the different conditions analyzed.

$$H_{bead} = H_{carboboride} \, x \, \%Carboboride + H_{M2B} \, x \, \%M2B + H_a \, x \, \%a + H_{Nbc} \, x \, \%Nbc \qquad (1)$$

From the results of phase percentages (Figure 7) and the measured microhardness values of the phases and considering 2440 HV for niobium carbide, the bead hardness was calculated with Equation 1. These calculated values were compared with the macroscopically measured values (HV2) on the last bead. The results obtained are shown in Figure 8.

It can be seen that the hardness of the deposit measured for all conditions presented a very good correlation with the values obtained from applying the mixture rule model. The macro hardness of the treated sample at 500 C° did not present significant modifications in respect of the AW. When the temperature increases up to 800 C° produced an approximate decrease of the 21% of hardness. At 900C° it has been seen an increase of the hardness up to 1130 HV in respect of the 940 HV in AW. Regarding the microhardness variations of the phases, a decrease can be seen up to 800 °C and a hardening for the treated test specimen at 900 °C. The microhardness of the $M_2B$ carboboride did not show significant modifications in all the test specimens, the values obtained being consistent with what was expected for this type of materials[34,35]. The decrease in microhardnes of the alpha-Fe phase up to 800 °C would be associated with the loss of solubilized elements, both interstitial and substitutional of the lattice[16-18]. Finally, for the test specimen treated at 900 °C, a strong increase in hardness was observed due to the formation of martensite and the presence of secondary carbides $M_6X$ and $M_{23}X_6$ (M: Cr, Fe; X: C, B)[35].

The micrographs in backscattered electron (BS) mode (Figure 9) show the increase of the indent area of the sample 800 respect to AW, which indicates a lower hardness. Likewise, the transgranular cracking of $M_2B$ borides can be seen in both conditions, and in 800 intergranular cracking with strong rupture of eutectic carboborides and $M_2B$, associated with a less hard matrix. In the sample 900 it has been seen small cracks. The length of these cracks has not exceeded the 10 microns. The niobium carbides located in the vertices of the indent area presented transgranular cracks. The interphase between the carbide $M_2B$ with the matrix, acted as the preferential place of cracks propagation. In all the samples it has been seen that the crack did not propagation in the matrix.
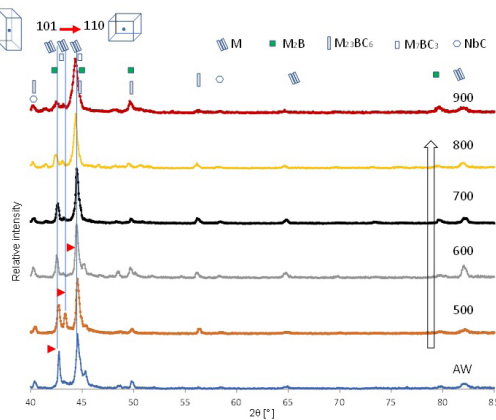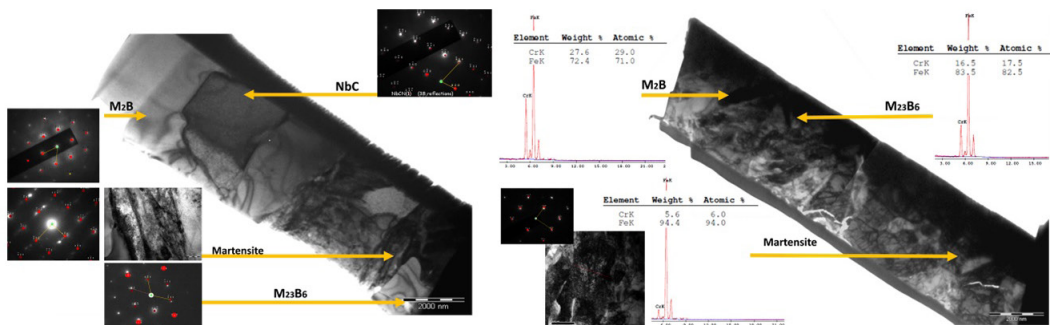


**Figure 6.** TEM images, electron diffraction patterns and EDS of the phases for AW and 500.

## 3.5. Wear

In Figure 10 the results of weight loss are presented, obtained from the ASTM G-65 wear tests carried out for the different conditions analyzed, depending on the hardness of the bead.

A good linear correlation was observed between weight loss and hardness. The test specimens heat-treated between 600° and 800°C presented a lower resistance to wear
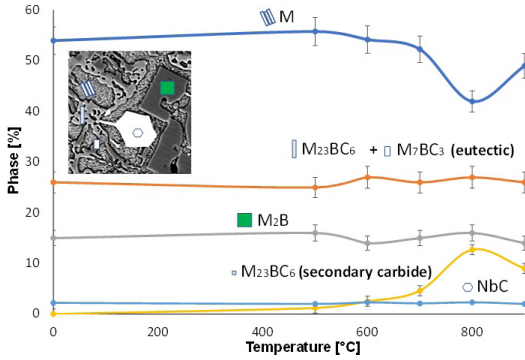


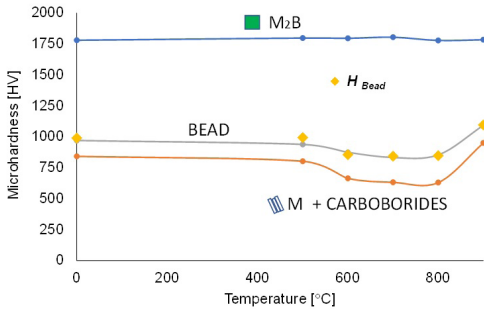**Figure 7.** Percentage of phases based on PWHT temperature.



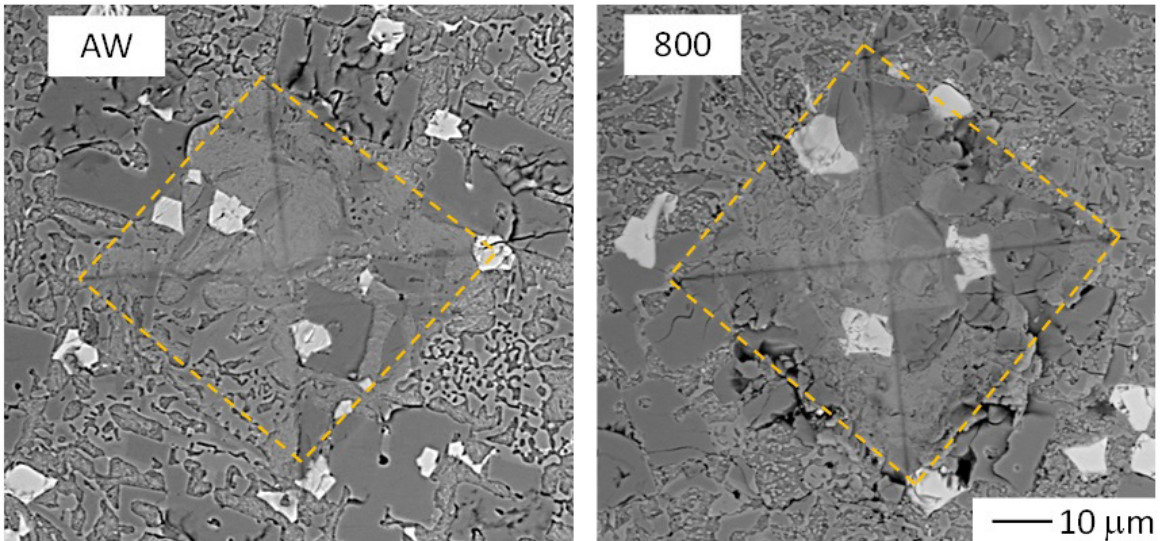**Figure 8.** Microhardness of the phases based on the PWHT temperature.

(30-40%), with respect to the AW condition. This would be associated with the decrease in the microhardness of the matrix, as shown in Figure 8. Furthermore, it was observed that the test specimens treated at 900 °C presented the best resistance to wear (% 30). It is important to remark that the value of wear resistance for the specimen 900 is close to the expensive nickel–tungsten carbide[36].

On the worn surface the presence of abrasion lines, in the direction of wear, produced by the scratching of the sand was detected. The average thickness of the grooves was between 1 and 20 µm, being greater for the softer test specimens. Figure 11 shows SEM-BS images. The analyzed area belongs to the center of the wear surface.

In hard coatings[35] the abrasive wear is controlled by the size, distribution and hardness of the phases. The sliding of the hard SiC particles over the surface produced on the microstructure: fragmentation, detachment and ploughing or microcutting, see Figures 11. The abrasive wear was produced in an irregular worn path with a big size, therefore it is considered as a heterogeneous. The plastic deformation level was too low with a lot of intergranular and transgranular cracks. In all the samples it has been seen plowing, on the other hand, in the samples of the Figures 11a and 11c it has been seen microcutting. As it is shown in the Figures 3, the path of the metallic phase α into the matrix is too short with respect of the depth identation of the abrasive particles. As a consequent, it unlikely to found deep grooves (sample 900). However, it has been found severe damages in the surface caused by ploughing and cutting in the samples where the hardness of matrix decreased.

The primary carboborides $M_2B$ in all the sample were oriented preferentially in perpendicular direction of the worn surface, being this one the higher wear resistance[35]. In all the cases it has been seen in the borides $M_2B$, fragmentation and cracks in the attack side of the hard particles, as it is shown in the Figures 11c and 11f. In some areas it has been seen elongated borides in oblique direction of the wear direction. In these cases, the transversal cracks were formed in direction
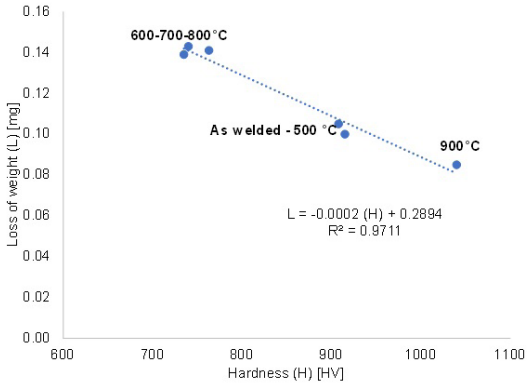


**Figure 9.** SEM-BS images of HV2 hardness imprints for AW and 800.

**Figure 10.** Weight loss based on the microhardness for the different conditions analyzed.

of the boride growth, see Figure 11b. This effect was higher when the carbides $M_2B$ were surrounded by the eutectics phases that present the less hardness.

The resistance to abrasive wear of the niobium carbides depended on the phases that surrounded them. In the sample 800, the niobium carbides were cracked and fragmented in small particles that were pull out of the matrix, decreasing its protection. On the other hand, when these carbides were found surrounded or inside the eutectic phase, it was produced a higher fragmentation than inside the $M_2B$.

On worn surface of sample 800, it can be seen cracks and fragmentation of $M_2B$ borides and niobium carbides and fractured eutectic carboborides. This is consistent with those observed in the area indenters (Figure 9) with the exception of the fracture of NbC. About the worn surface on samples treated at 600, 700 and 800°C, the softening of the matrix
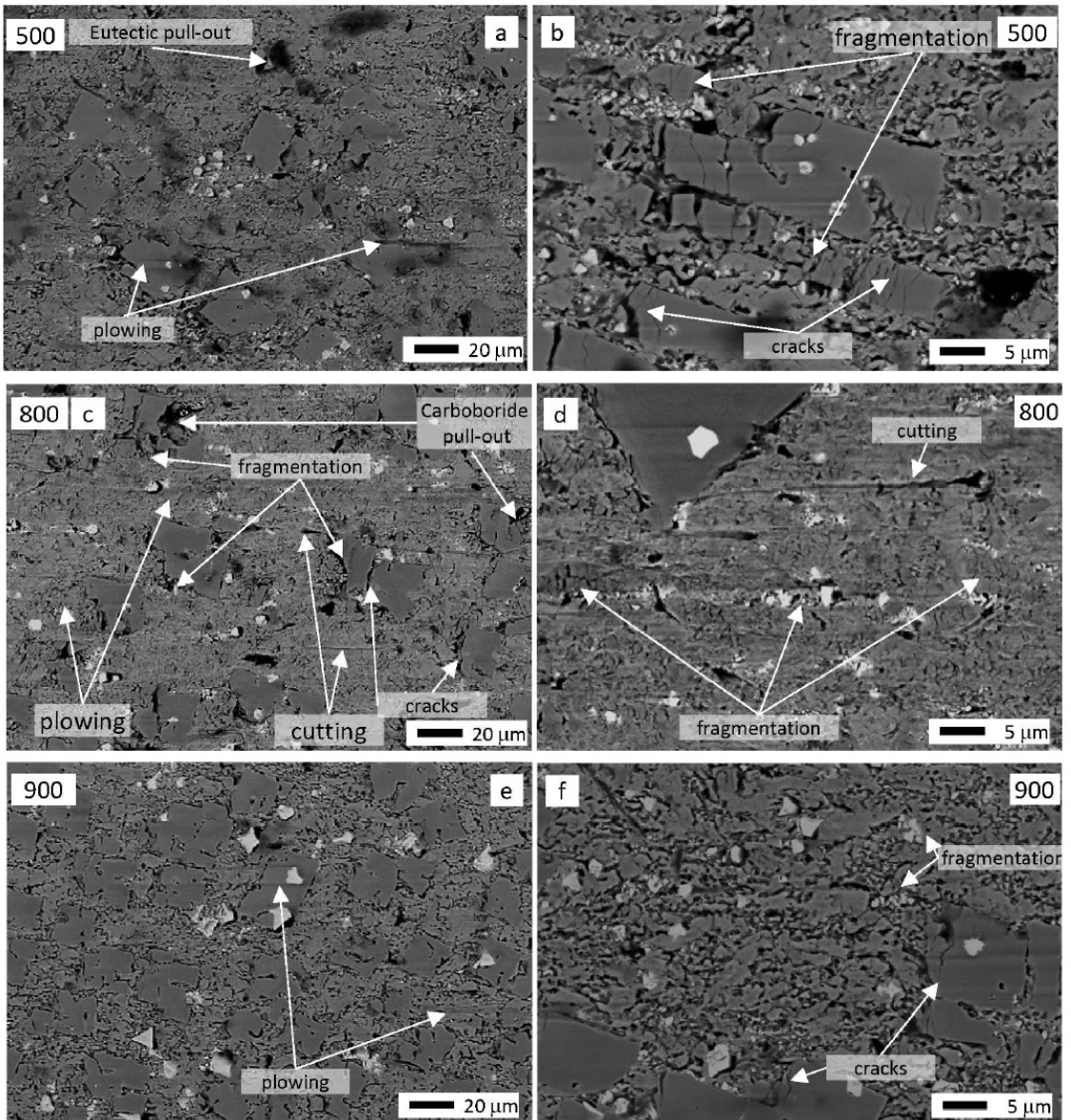


**Figure 11.** BSE mode images of the worn surface at a,b) 500, c,d) 800 and e,f) 900.

decrease the wear resistance and eutectic carboborides and the niobium carbide are worn by mechanisms of cutting, ploughing, fragmentation and spalling. This could be associated with the hard sand particles generated high stresses due to rolling and sliding on the phases, causing high damage and then the cracking and detachment of the carboborides and carbides[35-41]. With the increase in hardness, this effect decreased for the 500 test specimens and was significantly lower for the 900 sample.

## 4. Conclusions

- The weld metal obtained by FCAW welding presented a good surface finish, low levels of spatter and slag. Most of the beads cracked during cooling.
- The microstructure of the deposited metal (AW) was formed by a matrix of α'-Fe, $M_2B$ borides, metal carboborides $M_7(BC)_3$, $M_{23}(BC)_6$) and NbC, associated with the high concentration of alloying elements of the Fe- (Nb, Cr) - (C, B) system.
- In the heat-treated test specimens after welding between 500 and 800°C there was a thickening of the secondary carbides $M_{23}X_6$ and $M_6X$ (M: Cr, Fe; X: C, B) on the α-Fe matrix. In the test specimen treated at 900°C, a partial dissolution of the carbides and the thickening of the secondary carbides were observed.
- The hardness of the microstructure, presented a decrease up to 800°C and a hardening for the test specimen treated at 900°C, with respect to the AW condition. At 900°C, a strong increase in hardness was observed due to the presence of secondary carbides and martensite. A good fit of the measured values was obtained with a model based on the mixing rule.
- The test specimens heat-treated between 600 and 800°C presented lower resistance to wear (30-40%) and that the specimens 900°C presented an increase of %32 with respect to AW. A good correlation was observed between abrasive wear resistance and the hardness of the deposited metal.

## 5. Acknowledgment

## 6. References

1. Heath G. Nanotechnology and welding: actual and possible future applications. In: Proceedings of the Castolin-Eutectic Seminar. Brussels, Belgium; 2006. p. 25-35.

2. Badisch E, Kirchgaßner M, Polak R, Franek F. The comparison of wear properties of different Fe-based hardfacing alloys in four kinds of testing methods. Tribotest. 2008;14(4):225-33.

3. Branagan DJ, Marshall MC, Meacham BE. High toughness high hardness iron based PTAW weld materials. Mater Sci Eng A. 2006;428(1-2):116-23.

4. Branagan DJ, Tang Y. Development extreme hardness (>15 GPa) in iron-based nanocomposites. J Composites Part A. 2002;33:855-9.

5. Inoue A. Bulk amorphous alloys, preparation and fundamental characteristics. In: Inoue A, Hashimoto K, editors. Amorphous and nanocrystalline materials: advances in materials research. Berlin: Springler; 1998. Vol. 3.

6. Inoue A. Bulk glassy alloys, practical characteristics and applications. Zurich: Trans Tech Publications; 1999.

7. Inoue A. Stabilization of metallic supercooled liquid and bulk amorphous alloys. Acta Mater. 2000;48(1):279-306.

8. Norrish J. Advanced welding processes. Cambridge: Woodhead Publishing; 2006.

9. Chaus AS. Modifying Cast Tungsten-Molybdenum High-Speed Steels with Niobium, Zirconium, and Titanium. Metal Sci Heat Treat. 2005;47(1-2):53-61.

10. Khodabandeh AR, Jahazi M, Yue S, Aghdashi ST. The determination of optimum forging conditions for the production of high strength-high impact toughness automotive parts. Mater Manuf Process. 2006;21:105-10.

11. Ye T, Hanguang F, Jian L, Xingye G, Yongping L. Microstructure and properties of casting Fe–Cr–B alloy after quenching treatment. Trans Indian Inst Met. 2019;72(7):1823-35.

12. TeroMatec. Datasheet: TeroMatec 395NOA. USA: Eutectic Castolin-ESAB; 2015.

13. Degen T, Sadki M, Bron E, König U, Nénert G. The HighScore suite. Powder Diffr. 2014;29(S2):S13-8.

14. ASTM: American Society for Testing and Materials. ASTM-G65: standard test method for measuring abrasion using the dry sand/rubber wheel apparatus. West Conshohocken: ASTM; 2016.

15. Liu S, Zhou Y, Xing X, Wang J, Ren X, Yang Q. Growth characteristics of primary M7C3 carbide in hypereutectic Fe-Cr-C alloy. Sci Rep. 2016;6(1):32941.

16. Wang K, Li D. Formation of core (M7C3)-shell (M23C6) structured carbides in white cast irons: a thermo-kinetic analysis. Comput Mater Sci. 2018;154:111-21.

17. Branagan DJ. Engineering structures to achieve targeted properties in steels on a nanoscale level. Calphad: Comput Coupling Ph Diagr Thermochem. 2007;31(3):343-50.

18. Sorour AA. Understanding the solidification and microstructure evolution during CSC-MIG welding of Fe-Cr-B-based alloy. Mater Charact. 2013;86:127-38.

19. Matsubara Y, Sasaguri N, Shimizu K, Yu SK. Solidification and abrasion wear of white cast irons alloyed with 20% carbide forming elements. Wear. 2001;250:502-10.

20. Chen X, Li Y. Effect of heat treatment on microstructure and mechanical properties of high boron white cast iron. Mater Sci Eng A. 2010;528(2):770-5.

21. Guo C, Kelly P. Boron solubility in Fe–Cr–B cast irons. Mater Sci Eng A. 2003;352(1-2):40-5.

22. Liu Z, Chen X, Li Y, Hu K. Effect of chromium on microstructure and properties of high boron white cast iron. Metall Mater Trans, A Phys Metall Mater Sci. 2008;39(3):636-41.

23. Röttger A, Lentz J, Theisen W. Boron-alloyed Fe–Cr–C–B tool steels: thermodynamic calculations and experimental validation. Mater Des. 2015;88:420-9.

24. Christodoulou P, Calos N. A step towards designing Fe–Cr–B–C cast alloys. Mater Sci Eng A. 2001;301(2):103-17.

25. Lv Z, Fu H, Xing J, Ma S, Hu Y. Microstructure and crystallography of borides and mechanical properties of Fe–B–C–Cr–Al alloys. J Alloys Compd. 2016;662:54-62.

26. Budiansky B. Thermal and thermoelastic properties of isotropic composites. J Compos Mater. 1970;4:240-86.

27. Lesle P, Dong M, Soppa E. Simulation of inter-penetrating microstructures by self consistent matricity models. Scr Mater. 1998;38:1321-7.

28. Pederson OB. The elastic, thermoelastic and plastic behaviour of short fibre metal matrix. Acta Metall. 1983;31:1968-75.

29. Nardone VC. An analytical study on strengthening of particulate reinforced metal matrix composites. Acta Mater. 1996;4(1):69-77.

30. Shen YL. Effective elastic response of two-phase composites. Acta Metall Mater. 1994;42:77-97.

31. Dong M, Scmauder S. Modeling of metal matrix composites by a self-consistent embedded cell model. Acta Mater. 1996;44:2465-78.

32. Voigt W. About the relationship between the two constants of elasticity of isotropic bodies. Ann Phys. 1889;38:573-87.

33. Reuss A, Angew Z. Berechnung der fließgrenze von mischkristallen auf grund der plastizitätsbedingung für einkristalle. Appl Math Mech. 1929;9:49-58.

34. Lentz J, Röttger A, Großwendt F, Theisen W. Enhancement of hardness, modulus and fracture toughness of the tetragonal $(Fe,Cr)_2B$ and orthorhombic $(Cr,Fe)_2B$ phases with addition of Cr. Mater Des. 2018;156:113-24.

35. Bahoosh M, Shahverdi HR, Farnia A. Abrasive wear behavior and its relation with the macro-indentation fracture toughness of an fe-based super-hard hardfacing deposit. Tribol Lett. 2019;67(3):100.

36. Mendez PF, Barnes N, Bell K, Borle SD, Gajapathi SS, Guest SD, et al. Welding processes for wear resistant overlays. J Manuf Process. 2014;16(1):4-25.

37. Yüksel N, Şahin S. Wear behavior–hardness–microstructure relation of Fe–Cr–C and Fe–Cr–C–B based hardfacing alloys. Mater Des. 2014;58:491-8.

38. Zhang J. Effects of chromium addition on microstructure and abrasion resistance of Fe-B alloys. Tribol Lett. 2011;44:31-9.

39. Zhou YF, Qin GK, Jiang PJ, Wang SF, Qi XW, Xing XL, et al. Dry sliding wear behavior of (Cr, Fe)7C3-γ(Cr, Fe) metal matrix composite (MMC) coatings: the infuence of high volume fraction (Cr, Fe)7C3 carbide. Tribol Lett. 2018;66(3):108.

40. Kirchgaßner M, Badisch E, Franek F. Behaviour of iron-based hardfacing alloys under abrasion and impact. Wear. 2008;265(5–6):772-9.

41. Berns H. Comparison of wear resistant MMC and white cast iron. Wear. 2003;254(1-2):47-54.